STAND AND REAL-CONDITIONS TESTING OF AN AUTONOMOUS OPTICAL NAVIGATION SYSTEM FOR OPERATIONS IN CIRCUMLUNAR ORBITS

© 2025 B.S. Zhukov*, G.A. Avanesov, A.S. Liskiv, P.S. Smetanin
Space Research Institute RAS, Moscow 117997, Russia
**e-mail: bzhukov@mail.ru*

Received October 03, 2023
Revised November 29, 2023
Accepted November 29, 2023

Abstract. Stand testing of an autonomous optical navigation system for operation in circumlunar orbits and during Earth-Moon transfer was performed. The system includes a wide-angle navigation camera for estimation of spacecraft position using observations of the planet’s horizon and of ground control points on its surface, a narrow-angle navigation camera for refinement the SC position using ground control points in higher resolution images, and two star trackers for determination of system orientation. The navigation software was also tested using the image of the lunar surface obtained by the television system STS-L installed on the *Luna-25* spacecraft. All the control points from the developed catalog that were located in the imaged area were confidently recognized. The diversion in the spacecraft coordinates as obtained from the optical navigation measurements and from the ballistic forecast was within the expected measurement and forecast errors.

Keywords: *optical navigation, horizon, ground control point, stand testing, circumlunar orbit, STS-L, Luna-25*

DOI: 10.31857/S00234206250111e2

INTRODUCTION

Autonomous optical navigation is increasingly being used in the practice of space exploration of planets and small bodies of the Solar system. Traditional radio engineering methods (one-, two-, three-way Doppler radar, radio interferometry with ultra-long bases) require a certain amount of time spent on the propagation of the radio signal, on its ground processing and accumulation of measurements [1]. Autonomous optical navigation, which makes it possible to determine the position of a spacecraft by on-board image processing obtained by optical imaging systems, is indispensable in cases where it is required to automatically determine and correct the spacecraft's orbit in real time. Such a situation may occur during spacecraft launch into a near-planetary orbit and after orbit corrections, during automatic spacecraft landing on the surface of celestial bodies. In addition, the addition of autonomous optical measurements of navigation data obtained by ground-based radio engineering systems increases the reliability and safety of space missions, which is especially important for manned flights.

In domestic practice, television devices were first used for autonomous navigation in the Vega project in 1984-1986, when, during the spacecraft's passage past the nucleus of Halley's comet, the television system automatically guided the platform with scientific instruments in the center of brightness to the object of observation [2]. The same method was used to guide scientific equipment (using additional spacecraft rotation) using the AvtoNav autonomous optical navigation system developed at the Jet Propulsion Laboratory (USA) during the passage of small bodies (comets and asteroids) in the missions Deep Space 1, STARDUST, Deep Impact, EPOXI and STARDUST NExT [3].

To control the approach to Phobos and the landing of the descent vehicle on it (project “*Phobos-Grunt*”), including the selection of a safe landing site, a Television Navigation and Surveillance System (TNSS) was developed, consisting of two cameras - wide-angle and narrow-angle [4]. Unfortunately, due to the spacecraft accident, the TNSS never saw practical use.

Autonomous optical navigation on the descent trajectory when approaching the landing area was used in American missions *Mars* -2020 during landing on Mars (https://robotics.jpl.nasa.gov/what-we-do/flight-projects/mars-2020-rover/terrain-relative-navigation/) and *IM* -1 (*Intuitive Machines*) in 2024 during landing on the Moon (https://www.intuitivemachines.com/_files/ugd/7c27f7_51f84ee63ea744a9b7312d17fefa9606.pdf).

Autonomous selection of a safe landing site using television images was carried out during the landing on the lunar surface of the Chinese probes Chang'e 3–6 in 2013–2024 [5] and the Indian probe *Chandrayaan* -3 in 2023 (https://www.isro.gov.in/Chandrayaan3_Details.html), as well as the Chinese probe *Tianwen* -1 during landing on the surface of Mars in 2021 [6].

AUTONOMOUS OPTICAL NAVIGATION SYSTEM AND TEST BENCH FOR ITS DEVELOPMENT

Currently, taking into account the accumulated experience and prospective plans for flights of domestic spacecraft to the Moon, an autonomous optical navigation system [7] is being created at IKI RAS, which includes:

- a wide-angle navigation camera (ShNK), designed to determine the position of the spacecraft (SC) using the planet's horizon and control points (CP) — well-recognizable areas of the surface tied to the topographic model of the Moon;
- a narrow-angle navigation camera (UNK), designed to refine the position of the spacecraft using CPs, with higher resolution images;
- two star trackers, designed to determine the orientation of cameras;
- a data processing unit (DPU).

All devices are unified and are built on the basis of BOKZ family star trackers developed at IKI RAS. They differ only in objectives, light filters, and software. The characteristics of the optical heads (OH) of these devices are given in Table 1.

Table 1. Main parameters of optical heads of the autonomous optical navigation system

Characteristics	**Camera**		
	OH-ShNK	**OH-UNK**	**OH-ZD** (2 pcs.)
Focal length, mm	3.6	23	36
Frame size, pixels	2048 × 2048		
Angular resolution, arc sec	316	49.3	31.5
Field of view, arc deg	180	27.5	17.8
Spectral range, μm	0.8–0.9	0.8–0.9	0.5–0.9

For experimental development of the system at IKI RAS, a specialized test bench has been created [8], which includes several computers and display devices that allow reproducing images of the Moon, Earth, and stars at the scale and perspectives corresponding to the spacecraft position on the flight path (Fig. 1). The bench also includes a personal computer to which the optical heads OH-SD, OH-UNC, and OH-WFC can be connected either directly or through the BDP of the navigation system via an interface unit.

Fig. 1. Autonomous optical navigation technology test bench: top — WFC bench (left) and its projection part (right): 1) control computer monitors, 2) optical projector, 3) screen, 4) WFC optical head (covered with black cloth); bottom: left — projection part of the UNC bench with projection monitor (1) and collimator lens (2), right — recording part of the UNC bench with optical head (3)

The specified flight parameters are compared with the values measured by the navigation system instruments. In this process, the spacecraft orientation angles and coordinates in the body-fixed planetocentric coordinate system (PCCS) are compared. For the Moon, the Moon-ME (Mean Earth) is used as the PCCS, the center of which coincides with the center of mass of the Moon, the Z axis is directed along the mean direction of the Moon's rotation axis, the X axis lies in the mean equatorial plane and is directed to the initial meridian (toward Earth), the Y axis also lies in the equatorial plane and completes the right-handed system. The radius of the Moon's reference sphere is taken as $R_0 = 1737.4$ km. The spacecraft coordinates are displayed both as Cartesian coordinates, which are directly used in dynamic filtering of navigation measurements when determining the spacecraft orbit, and for convenience as spherical coordinates — latitude and longitude of the subsatellite point (SSP) and spacecraft altitude.

Thus, the equipment and the software and mathematical support of the stand allow both to simulate the conditions of shooting celestial bodies and to evaluate the results of the navigation system instruments.

Before the start of each "flyby," an automatic geometric calibration of the stand is performed, based on projecting a regular grid of points onto the monitor screens, capturing it, recognizing the grid points on the obtained images, and determining the geometric parameters that link the coordinates of points in the images sent to the monitor screens and their coordinates in the images obtained by the cameras. The calibration of the stand is checked during the "flyby," and if it changes due to warming up of the stand, the "flyby" is repeated.

MODELING LUNAR IMAGES

Lunar images significantly depend on the direction of sunlight falling on its surface and the direction of observation. At a phase angle (angle between the directions of incidence and observation) greater than ~40º, at which navigation by reference points is planned to be implemented, the main factor affecting the image structure is the relief. At such phase angles, variations in the microstructure of the regolith, which have a dominant influence on the brightness distribution of the lunar surface at small phase angles, can be neglected. At phase angles less than 40º, only horizon navigation is planned, for which adequate modeling of the brightness distribution across the lunar disk is not essential.

Lunar images were modeled in real time using the global topographic model GLD100-256P with a surface resolution of about 118 m (https://wms.lroc.asu.edu/lroc/view_rdr/WAC_GLD100). The GLD100 model was built from images obtained by the Wide Angle Camera (WAC), which is part of the LROC (Lunar Reconnaissance Orbiter Camera) imaging system on the *Lunar Reconnaissance Orbiter* (*LRO*) [9]. At near-polar latitudes, it is supplemented by the LOLA-256P model, built from data from the LOLA (Lunar Orbiter Laser Altimeter) laser altimeter on the same spacecraft . The brightness distribution of the lunar surface was calculated using the Hapke model [10], with the average values of its parameters for the Moon. Although there are maps of the distribution of Hapke model parameters across the lunar surface [11], their resolution of 5° (150 km) is not sufficient for modeling orbital images.

When constructing the image displayed on the stands, the geometric model of the camera and the stand calibration results were taken into account so that the angular distribution of the brightness field at the camera aperture corresponded to the actual distribution of the Moon's brightness field under the given observation conditions.

The adequacy of lunar image modeling was verified by comparing model images with real images obtained by the WAC/LROC camera.

SOFTWARE AND ALGORITHMIC SUPPORT FOR NEAR-PLANETARY NAVIGATION

At the first stage of processing, the spacecraft position is determined using the horizon from wide-angle camera images, using the algorithm described in [12]. For this purpose, potential horizon points are identified in the image using the Sobel operator, terminator points are filtered out, and the directions to the remaining horizon points are approximated by a circular cone. The direction of the cone axis gives the direction to the center of the Moon in the internal coordinate system (ICS) of the camera. It is transformed into the Moon-ME lunar coordinate system using data on the camera orientation in the J2000 inertial coordinate system, measured by star trackers, and using the transformation from J2000 to Moon-ME for a specified time. Thus, the position of the sub-satellite point is determined. The spacecraft altitude is estimated based on the aperture angle of the approximating cone.

Preliminary estimates of TSP coordinate determination errors on the horizontal for low orbits are ~10 km, height errors ~1 % (3σ), which is quite sufficient for proceeding to the next stage - refining the spacecraft position using control points. For this purpose, the central part of the wide-angle camera's field of view is used, where observation angles do not exceed 45°, and consequently, geometric distortions are not too large. The search radius at the first stage is set to 10 km, and control points that may fall within the central part of the camera's field of view are selected from the catalog. Then, a search area with a radius of 10 km is formed in the geometric projection of the control points, and they are searched using a multi-scale matching method. The control points are first searched in coarsened images, and then their position is refined using the original image. Beforehand, reference images of the control points are calculated based on their 3D models for given resolution parameters and illumination and observation directions.

To limit computation time, no more than 10 control points are sought in the image, positioned closest to the calculated intersection point of the camera's optical axis with the Moon's reference sphere. When at least two control points are identified in the image, and the direction vectors to them in the camera coordinate system and the transformation of direction vectors to the PCSC are determined, the spacecraft's radius vector in the PGCS is found [13]. Geometrically, this procedure can be interpreted as finding, by the least squares method, the intersection point of rays constructed from the specified control points in directions opposite to their observation directions from the spacecraft (a method known in geodesy as resection).

Navigation uses a catalog of control points on the Moon, which was formed using the GLD100-256P lunar topographic model. For each control point, the catalog contains the characteristics of the control point (the radius vector of the control point in the PCSC, values of the control point quality criterion, etc.) and a multi-scale pyramid of 3D models of the control point with 5 levels. The resolution element size of the pyramid levels sequentially increases by a factor of two from 118 m for the most detailed level to 1888 m for the coarsest. The average distance between control points is 30 km, with the selection criterion being the maximization of the Harris criterion [14], averaged across pyramid levels, at solar phase angles greater than 40°.

The total volume of the catalog is over 70 thousand CPs.

Preliminary error assessment of spacecraft position estimation using reference points with WNS is approximately 1 km (3σ).

Further increase in measurement accuracy using CPs is possible with higher resolution images obtained by NNS (provided they capture a sufficient number of CPs). The search radius for CPs in NNS images is determined by the error in determining the lunar surface point position from WNS images. Transitioning from WNS to NNS when navigating by CPs improves spacecraft coordinate determination accuracy by an order of magnitude. However, the spacecraft altitude estimation error does not significantly decrease due to insufficient intersection angle (the angle between directions to the found CPs), limited by the NNS field of view of 27.5°.

RESULTS OF LABORATORY NAVIGATION MEASUREMENTS IN LUNAR ORBITS

For the experiments, polar orbits with altitudes of 70, 100, 200, 400, and 800 km were selected, starting above the Moon's north pole and passing over the intended landing site of the " *Luna* -25" spacecraft to the north of the Boguslavsky crater (69.545° S, 43.544° E). The coordinates of the subsolar point 1.0° N, 119.3° E were also chosen to correspond to the landing conditions of the " *Luna* -25" spacecraft. Under these conditions, observation is conducted at low Sun elevation, which is about 15° near the equator and decreases to 4° at 78° latitude. At lower Sun elevation, measurements using control points are not conducted due to excessive shadowing. Horizon measurements are conducted until the spacecraft disappears behind the terminator.

The resolution of WNS and NNS at these orbits and their field of view used for CP detection are shown in the table. 2. In the case of NFC, the entire field of view is used for detecting RPs, while in the case of WFC, its central part is used, corresponding to viewing angles within ±45°. The full field of view of the WFC within ±90° is used for horizon navigation measurements. At orbits below 200 km, the resolution of the NFC is significantly better than the resolution of RPs (118 m), and the field of view becomes comparable to the size of the RP determination area, resulting in an insufficient number of RPs usually appearing in the NFC field of view. Therefore, the transition to navigation measurements using RPs from WFC to NFC occurs at an altitude of 200 km. At higher altitudes, WFC measurements are conducted only by horizon.

Table 2. Resolution and field of view of WFC and NFC in polar orbits

Altitude, km	**WFC**		**NFC**	
	Resolution, m	**Field of view (± 45°), km**	**Resolution, m**	**Field of view, km**
70	107	140	17	34

100	153	200	24	48
200	307	400	48	96
400	614	800	96	192
800	1230	1600	192	384

Fig. 2 shows examples of WFC and NFC images obtained on the test bench, with the results of horizon arc determination and identified reference points on its surface.

Table 3 shows the proportion of WFC and NFC images in which the number of identified RPs was sufficient for navigation measurements. At an altitude of 200 km, the proportion of NFC images for which RP measurements could not be performed was 3 %, and at higher altitudes — 1 %. At altitudes below 200 km, the WFC was able to identify a sufficient number of RPs in all images, while at altitudes above 200 km, RP recognition sharply deteriorated due to insufficient resolution of the WFC test bench.

Fig. 2. Examples of WFC (top) and NFC (bottom) images obtained on the test bench from an altitude of 200 km; horizon points identified in the WFC image and reference points in both WFC and NFC images are marked in yellow

Table 3. Ratio of the number of images used for measurement by control points to the total number of images

Camera	**Height, km**				
	70	**100**	**200**	**400**	**800**
WNA	172 / 172	250 / 250	296 / 297	–	–
NNA	–	–	287 / 297	264 / 267	275 / 277

Errors in measuring spacecraft coordinates in lunar orbits are shown in Fig. 3–5, and their root mean square deviations (RMSD) — in Table 4. They are presented in the coordinate system RNB, where the axis R is directed along the radius vector of the spacecraft, the axis N — in the orbital plane perpendicular to the radius vector in the direction of spacecraft movement, the axis B — perpendicular to the orbital plane and complements the system to make it right-handed. The error along the R axis equals the error in height H. For a polar orbit, the N axis is directed approximately along the meridian, the B axis — along the parallel. Since the SSP is determined as the intersection point of the spacecraft radius vector with the lunar surface, the errors in the SSP coordinates are obtained by multiplying the errors in the spacecraft coordinates N and B by the coefficient $R_0/(R_0+H)$, equal to the ratio of the distances from the SSP and the spacecraft to the center of the Moon.

Table 4. Root Mean Square Errors of Test Measurements of Spacecraft Coordinates in Near-Moon Orbits (m)

Measurement Type	**Axis**	**Altitude, km**				
		70	**100**	**200**	**400**	**800**
WNS by horizon	R (H)	660	722	1300	1311	1937
	N	2740	2362	2168	1746	1661

	B	2977	2663	2874	1547	2089
WNS by control points	R (H)	183	315	717	–	–
	N	106	155	417	–	–
	B	100	139	276	–	–
UNS by control points	R (H)	–	–	185	220	411
	N	–	–	29	24	50
	B	–	–	35	26	46

Fig. 3. Errors ΔN, ΔB, ΔR of test measurements of spacecraft coordinates using WNS by horizon in near-Moon polar orbits at altitudes of 70, 100, 200, 400, and 800 km

Fig. 4. Errors ΔN, ΔB, ΔR of test measurements of spacecraft coordinates using WNS by control points in near-Moon polar orbits at altitudes of 70, 100, and 200 km

The standard deviation of errors for WNS by horizon does not exceed 2-3 km, and their maximum value is within 10 km (Fig. 3). Errors in altitude measurement by horizon increase with altitude. However, errors in the horizontal plane (NB) generally decrease, which is associated with a decrease in sensitivity to the horizon relief (on the Moon, the surface height difference relative to the reference sphere reaches ~10 km). The influence of the relief also determines the large autocorrelation interval of horizon errors, i.e., their slow change along the flight path.

Errors of WNS by control points in the horizontal plane are an order of magnitude smaller than those by horizon (Fig. 4). Their standard deviation does not exceed several hundred meters, with a maximum within 1 km. Altitude errors are approximately twice as large as those in the horizontal plane. Errors at control points generally increase with altitude and are weakly correlated along the orbit.

At altitudes of 200 km and above, the standard deviation of narrow-angle camera errors at control points in the horizontal plane is about 50 m, and the maximum errors do not exceed 200-300 m (Fig. 5). Altitude errors in this case are almost an order of magnitude larger due to the limited angular field of view of the narrow-angle camera.

Fig. 5. Errors ΔN, ΔB, ΔR of bench measurements of spacecraft coordinates using narrow-angle camera at control points on near-lunar polar orbits with altitudes of 200, 400, and 800 km

RESULTS OF FIELD NAVIGATION MEASUREMENTS BASED ON LUNAR SURFACE IMAGE OBTAINED BY THE STS-L CAMERA ON "*LUNA* -25" SPACECRAFT

Using the KAM-S television camera, which is part of the service television system (STS-L) on the " *Luna* -25" spacecraft, an image of the lunar surface in the area of the Zeeman crater

(75°05′ S, 135°05′ W) was obtained on August 17, 2023 from a near-lunar circular orbit with an altitude of about 100 km (Fig. 6). The KAM-S has the same matrix photoreceiver with dimensions of 2048 × 2048 pixels as the wide-angle and narrow-angle cameras, and with its 50° field of view, it occupies an intermediate position between them. From the specified altitude, the KAM-S resolution was about 93 m, with a frame size of 93 × 93 km. Data from ground-based geometric calibration of the camera were used in processing.

This image was used for:

- verifying the adequacy of lunar surface image simulation using the GLD100-256P topographic model;
- checking the recognizability of control points using reference images built from the GLD100-256P topographic model;
- evaluating the accuracy of spacecraft coordinate determination.

When applying the software-algorithmic support developed on the stand to the obtained image of the Moon, all 10 control points falling within the frame field were recognized. In 9 out of 10 cases, the correspondence of control points was found for all three resolution levels of reference images of control points built from their 3D models, and in one case - for two levels except the most detailed one. This confirms the adequacy of the choice of both the lunar surface model and the Harris criterion used in catalog construction, which gives preference to control points with pronounced texture throughout their definition window, rather than, for example, small craters on a quasi-homogeneous background, which the eye might probably choose, but which may be lost at the initial stage of recognition using roughened images.

Fig. 6. Image of the lunar surface obtained on 17.VIII.2023 by the KAM-S/STS-L camera. White nested squares show the found control points at three resolution levels of their reference images

The coordinates of the spacecraft in the PCSK, determined by the found control points using spacecraft orientation data, are compared with the ballistic forecast data (Table 4). The given root-mean-square errors of spacecraft coordinate determination from the image, estimated from the residual deviations of the reverse intersection method, are about 70 m for coordinates X and Y and about 200 m for coordinate Z, which is consistent with the errors of stand measurements. However, the discrepancy with the results of the ballistic forecast is significantly larger. In PCSK coordinates, it reaches 1.8 km, and in *RNB* coordinates it is: $\Delta N = 0.28$ km, $\Delta B = 1.5$ km, $\Delta R = 1.6$ km. This discrepancy may be related to errors in the ballistic forecast of the spacecraft position, which are estimated at ~1 km, and the error in binding the shooting time to the onboard time - up to 1 s, which leads to an error along the flight path of up to 1.6 km. It should be noted here that the STS-L on the "*Luna*-25" spacecraft was not tasked with navigation measurements, and therefore the time binding accuracy necessary for this purpose (~1 ms) was not provided.

Table 5. Comparison of spacecraft coordinate estimates in PCSK based on ballistic prediction and STS-L/CAM-S image processing results

	X, km	Y, km	Z, km	H, km
Ballistic data	–299.974	–267.074	–1788.522	95.664
Based on STS-L image	–298.160±0.069	–266.860±0.069	–1787.217±0.208	94.064±0.201

CONCLUSION

Testing of the autonomous optical navigation system was carried out on a specialized test bench. The obtained results confirmed the preliminary estimates of the navigation measurement accuracy and the methodology of interaction between measurements performed by wide-angle and narrow-angle navigation cameras in lunar orbits.

As a result of processing the lunar surface image taken by STS-L from the spacecraft "*Luna* -25", confirmation was obtained of reliable recognition of control points from the developed catalog, as well as confirmation of the correctness of the research and testing methods used during ground testing of the optical system for planetary navigation. The discrepancy between the navigation measurement results from the image and the ballistic prediction data was within the limits of measurement errors and ballistic prediction.

REFERENCES

1. Ground control complex for deep space vehicles. Development prospects. Ed. by Yu.M. Urlichich. Moscow: Radiotekhnika, 2012. 216 p.

2. Television imaging of Halley's comet. Ed. by R.Z. Sagdeev. Moscow: Nauka, 1989. 295 p.

3. *Bhaskaran S.* Autonomous navigation for deep space missions // Proc. Conf. American Institute of Aeronautics and Astronautics. Stockholm, Sweden. 2012. AIAA-2012-1267135. DOI: 10.2514/6.2012-1267135.

4. *Avanesov G.A., Gordeev R.V., Grishin V.A. et al.* Television system for navigation and observation // Astronomicheskiy vestnik. 2010. Vol. 44. No. 5. P. 473–479.

5. *Wang Q., Liu J.* A Chang'e-4 mission concept and vision of future Chinese lunar exploration activities // Acta Astronautica. 2016. V. 127. P. 678–683. DOI: 10.2016/j.actaastro.2016.06.024.

6. *Huang X., Xu C., Hu J. et al.* Powered-descent landing GNC system design and flight results for Tianwen-1 mission // Astrodynamics. 2022. V. 6. № 1. P. 3–16. DOI: 10.1007/s4/2064-021-0118-9/

7. *Avanesov G.A., Zhukov B.S., Smetanin P.S., Mikhailov M.V.* Testing the technology of autonomous navigation of deep space spacecraft on the International Space Station // Modern problems of remote sensing of the Earth from space. 2020. V. 17. № 7. P. 41–49. DOI: 10.21046/2070-7401-2020-17-7-41-49

8. *Avanesov G.A., Zhukov B.S., Smetanin P.S.* Test bench for developing the technology of autonomous near-planet optical navigation of spacecraft // Modern problems of remote sensing of the Earth from space. 2021. V. 18. № 3. P. 107–117. DOI: 10.21046/2070-7401-2021-18-3-107-117.

9. *Scholten F., Oberst J., Matz K.-D. et al.* GLD100: the near-global lunar 100 m raster DTM from LROC WAC stereo image data // J. Geophys. Res. 2012. V. 117(E12). DOI: 10.1029/2011JE003926 .

10. *Hapke B.W.* Theory of Reflectance and Emittance Spectroscopy. N.Y.: Cambridge Univ. Press, 2012.

11. *Sato H., Robinson M.S., Hapke B. et al.* Resolved Hapke parameter maps of the Moon // J. Geophysical Research: Planets. 2014. V. 119. Iss. 8. P. 1775–1805. DOI: 10.1002/2013JE004580

12. *Zhukov B.S., Zhukov S.B., Forsh A.A.* Possibilities of navigation measurements along the Earth's limb in visible and near-IR range // Modern problems of remote sensing of the Earth from space. 2015. V. 12. № 2. P. 61–76.

13. *Zhukov B.S., Polyansky I.V., Zhukov S.B.* Autonomous optical navigation in lunar orbits and during landing on the Moon using an ultra-wide-angle camera // Modern problems of remote sensing of the Earth from space. 2017. V. 14. № 2. P. 24–35. DOI: 10.21046/2070-7401-2017-14-2-24-35

14. *Harris C., Stephens M.* A combined corner and edge detector // Proc. 4th Alvey Vision Conference. Manchester, UK. 1988. P. 147–151. DOI:10.5244/C.2.23.

Fig. 1. Test stand for autonomous optical navigation technology development: top - SNK stand (left) and its projection part (right): 1) control computer monitors, 2) optical projector, 3) screen, 4) SNK optical head (covered with black cloth); bottom: left - projection part of the UNK stand with projection monitor (1) and collimator lens (2), right - recording part of the UNK stand with optical head (3)

Fig. 2. Examples of images obtained on the SNK (top) and UNK (bottom) test stands from an altitude of 200 km; highlighted in yellow are the identified horizon points on the SNK image and control points on the SNK and UNK images

Fig. 3. Errors ΔN, ΔB, ΔR of test stand measurements of spacecraft coordinates using SNK by horizon on near-lunar polar orbits at altitudes of 70, 100, 200, 400 and 800 km

Fig. 4. Errors ΔN, ΔB, ΔR of test stand measurements of spacecraft coordinates using SNK by control points on near-lunar polar orbits at altitudes of 70, 100 and 200 km

Fig. 5. Errors ΔN, ΔB, ΔR of test stand measurements of spacecraft coordinates using UNK by control points on near-lunar polar orbits at altitudes of 200, 400 and 800 km

Fig. 6. Image of the lunar surface obtained on 17.VIII.2023 by the KAM-S/STS-L camera. White nested squares show the identified control points at three resolution levels of their reference images

Fig.1

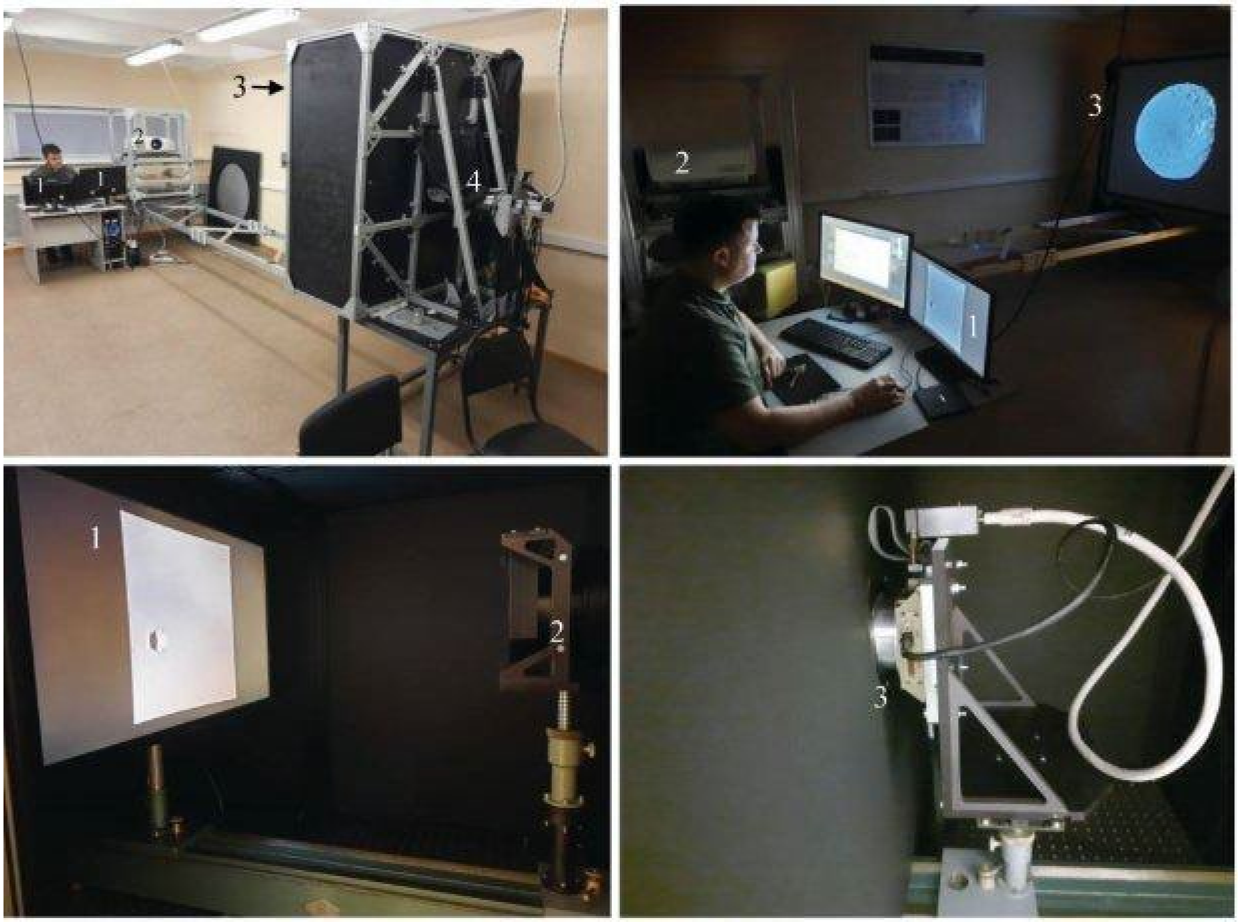

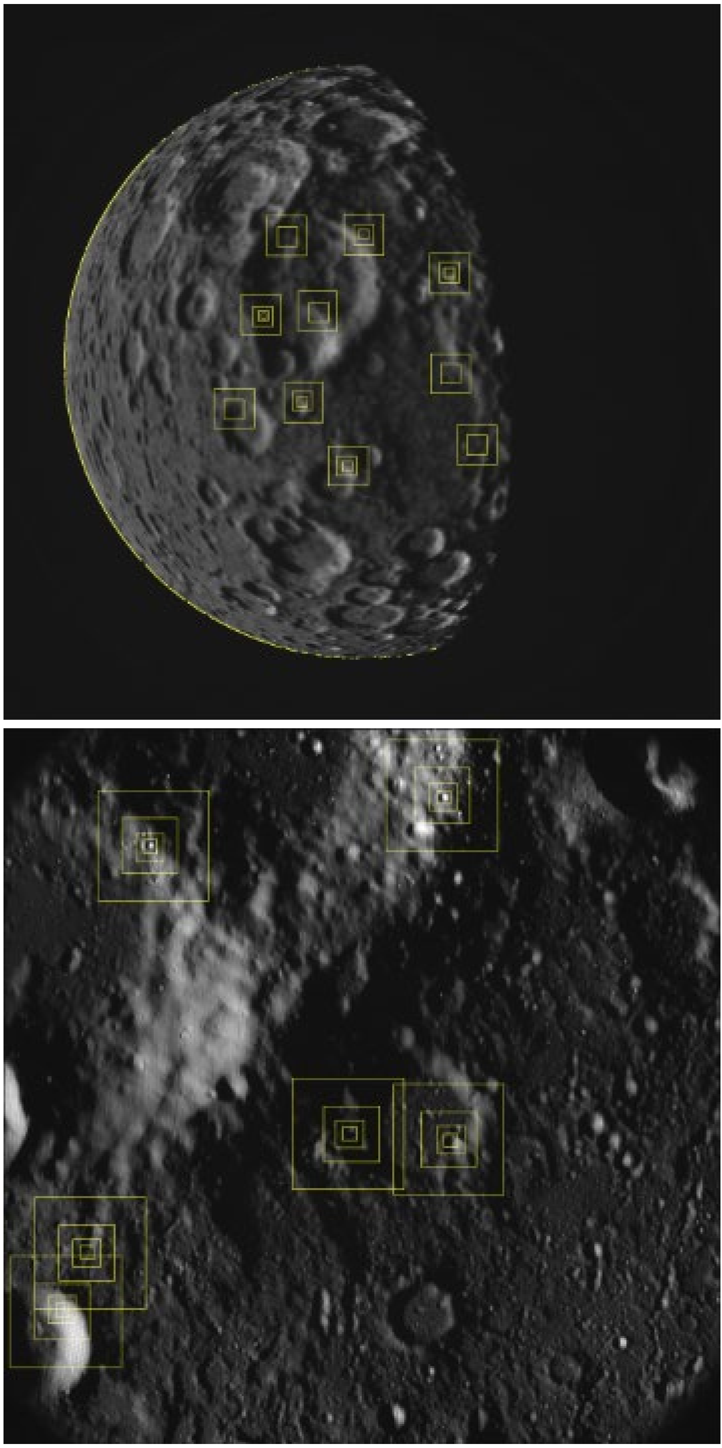

Fig.2

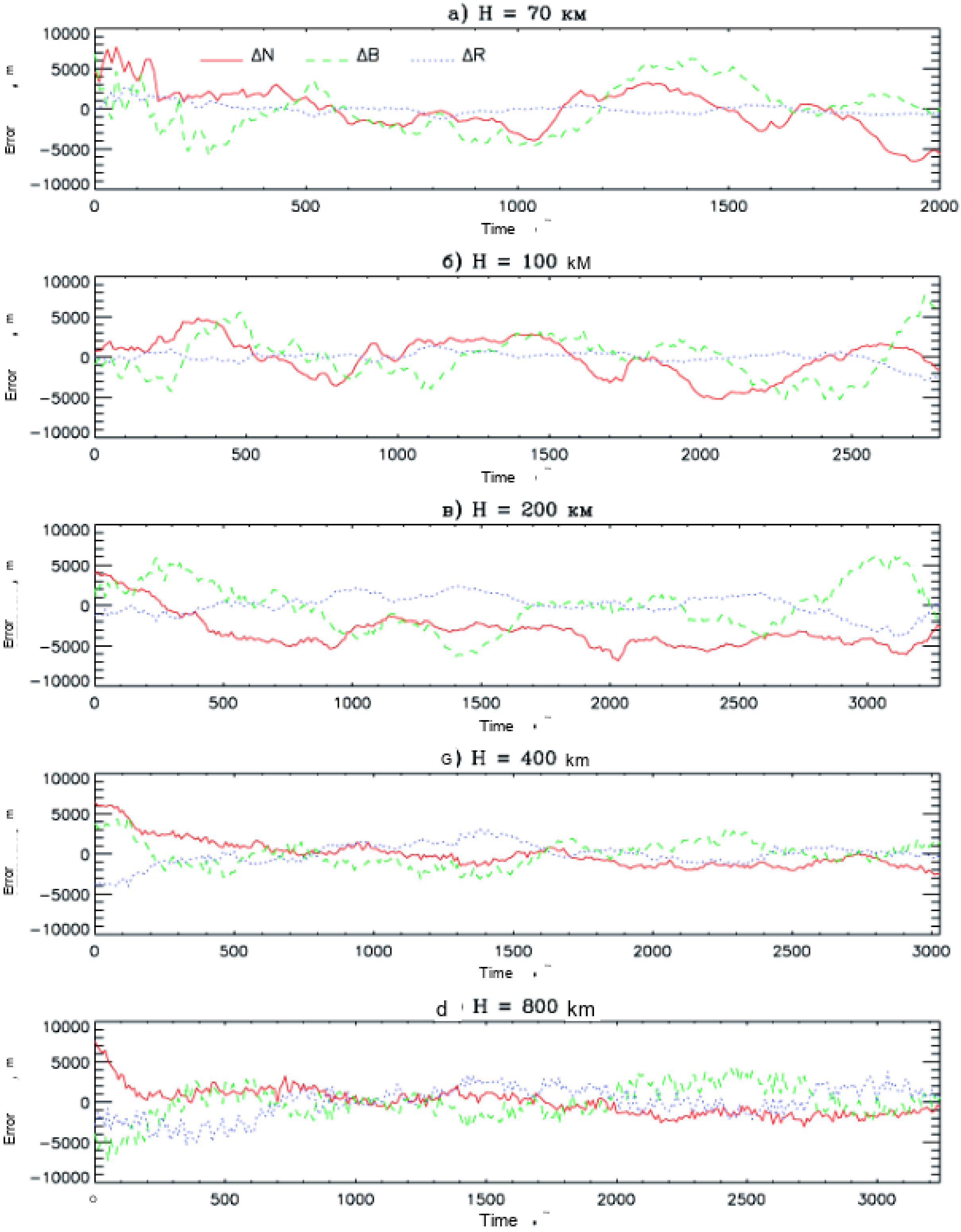
a) H = 70 км
ΔN
ΔB
ΔR
Error , m
10000
5000
0
−5000
−10000
0
500
1000
1500
2000
Time
б) H = 100 кМ
Error , m
0
500
1000
1500
2000
2500
Time
в) H = 200 км
Error , m
0
500
1000
1500
2000
2500
3000
Time
G) H = 400 km
Error , m
0
500
1000
1500
2000
2500
3000
Time
d H = 800 km
Error , m
0
500
1000
1500
2000
2500
3000
Time

Fig. 3

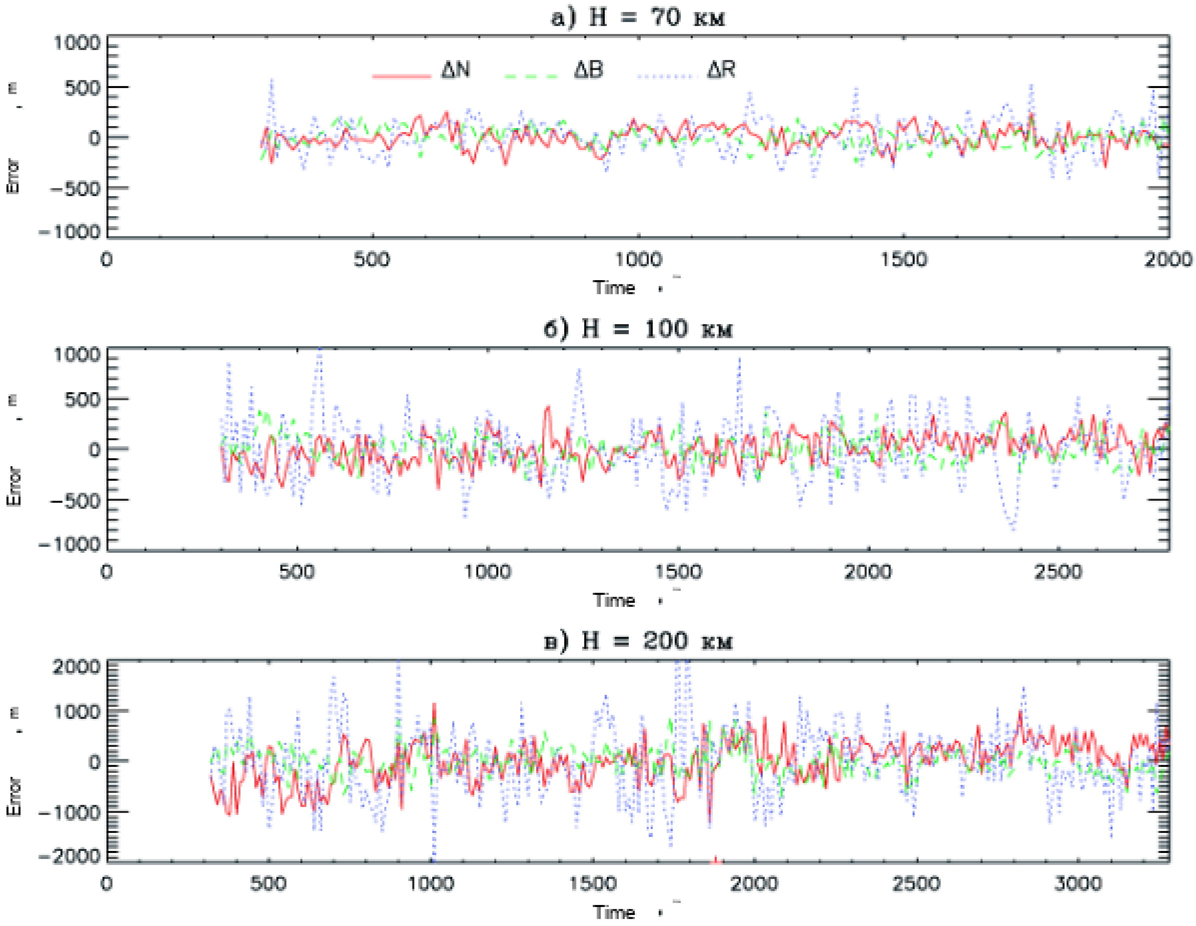

а) H = 70 км

б) H = 100 км

в) H = 200 км

Fig. 4

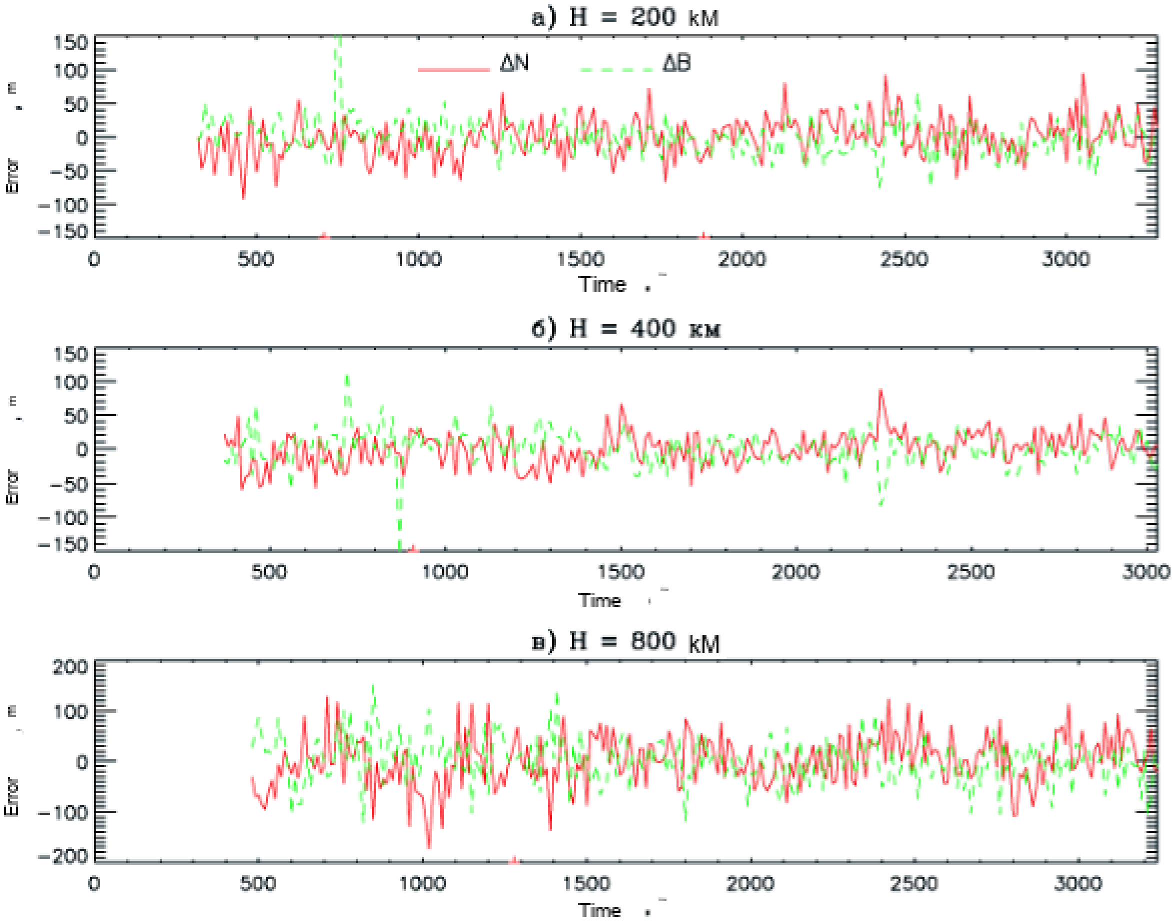
a) H = 200 kM
ΔN
ΔB
Error , m
Time
б) H = 400 км
Error , m
Time
в) H = 800 kM
Error , m
Time
150
100
50
0
−50
−100
−150
200
−200
0
500
1000
1500
2000
2500
3000

Fig. 5

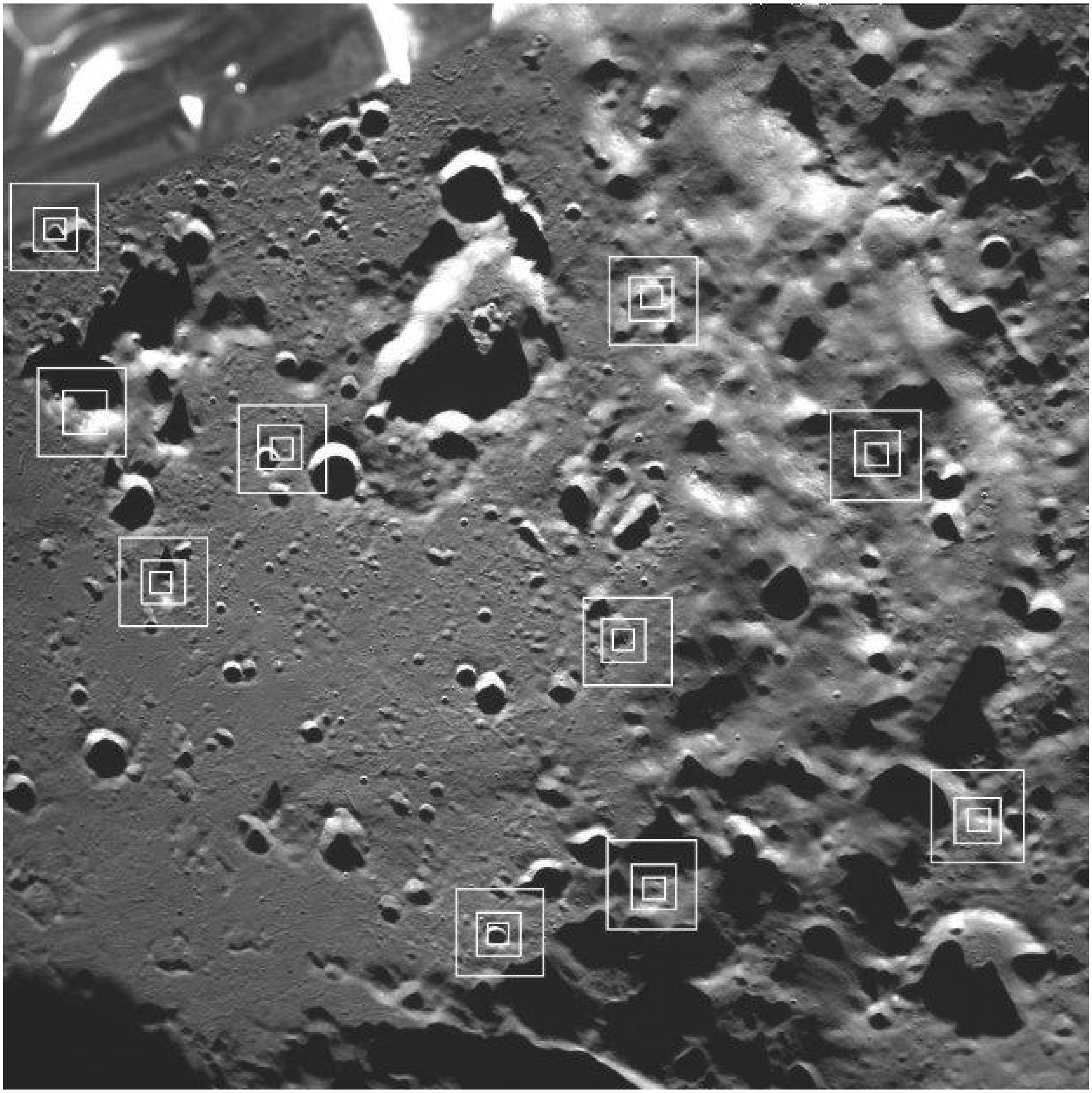

Fig. 6